

Progressively Exposing Active Facets of 2D Nanosheets toward Enhanced Pseudocapacitive Response and High-Rate Sodium Storage

Xin Xu, Ruisheng Zhao, Bo Chen, Lishu Wu, Chenji Zou, Wei Ai, Hua Zhang, Wei Huang,* and Ting Yu*

Sodium-ion batteries are gradually regarded as a prospective alternative to lithium-ion batteries due to the cost consideration. Here, three kinds of tin (IV) sulfide nanosheets are controllably designed with progressively exposed active facets, leading to beneficial influences on the Na⁺ storage kinetics, resulting in gradient improvements of pseudocapacitive response and rate performance. Interestingly, different forms of kinetics results are generated accompanying with the morphology and structure evolution of the three nanosheets. Finally, detailed density functional theory simulations are also applied to analyze the above experimental achievements, proving that different exposed facets of crystalline anodes possess dissimilar Na⁺ storage kinetics. The investigation experiences and conclusions shown in this work are meaningful to explore many other proper structure design routes toward the high-rate and stable metal-ions storage.

Owing to the rapidly increasing consumption market of lithium-ion batteries (LIBs), as well as the relative low abundance and uneven distribution of lithium resources, sodium-ion batteries

well as leading to the severe volume change during the cyclic Na⁺ storage processes, which cause the sluggish charging procedure and unavoidable capacity decay of NIBs.^[9] Along with the rapid development of nanotechnology in the past decades, porous and hierarchical materials with nanometre-sized structure are often synthesized and applied for battery electrodes.^[10–13] The size-decreased active material is able to increase the contact area with electrolyte, provide more surface for charge storage, and minimize the Na⁺ diffusion distance simultaneously, therefore resulting in high specific capacity and fast ion transportation to a certain extent.

On the other hand, the crystalline material with nanoscale structure can strengthen the capability of solvated Na⁺ storage arising at its surface and/or near surface, which is called as pseudocapacitance or surface-controlled process.^[14,15] The related kinetics analysis based on the pseudocapacitance response also offers a relatively accurate quantitative method to obtain more information for Na⁺ diffusion and storage, which can be used as guide to prepare more favorable nanostructures for high-rate electrodes.^[16,17] Particularly, for a crystalline material, the nanoscale structure obtained by size-decreasing route also represents the exposing intrinsic facets compared to the bulk material.^[18] Thus, it is believed that the enhanced pseudocapacitance response generated from surface-increased nanoscale material is essentially associated with the exposed active facets. Due to the anisotropic lattice adopted by crystalline material, it is apparent that different exposed facets will give rise to dissimilar influence on the pseudocapacitive contribution. Very recently, in LIB field, several inspiring works

(NIBs) gradually become a kind of prospective alternative energy storage device in the near future.^[1,2] In the academic field, the electrochemical performances of the reported cathode materials for NIBs are comparable to the corresponding counterparts for LIBs.^[3] Thus, the main challenge for the sodium-storage issue is gradually pointing to relieve the inherent drawbacks of the appropriate anode materials.^[4] Up to now, different types of anode materials with alloying, conversion, and intercalation Na⁺ storage mechanism are investigated toward realizing better performance.^[5–8] However, the close-packed crystal structures possessed by these anodes bring in considerable energy barrier for the Na⁺ solid-state diffusion, as


Dr. X. Xu, Dr. W. Ai, Prof. W. Huang
Shaanxi Institute of Flexible Electronics (SIFE)
Northwestern Polytechnical University (NPU)
Xi'an 710072, China
E-mail: iamwhuang@nwpu.edu.cn

Dr. X. Xu, L. Wu, Dr. C. Zou, Prof. T. Yu
Division of Physics and Applied Physics
School of Physical and Mathematical Sciences
Nanyang Technological University
Singapore 637371, Singapore
E-mail: yuting@ntu.edu.sg

Dr. R. Zhao
Department of Applied Chemistry
School of Science
Xi'an Jiaotong University
Xi'an 710049, China

Dr. B. Chen, Prof. H. Zhang
School of Materials Science and Engineering
Nanyang Technological University
Singapore 639798, Singapore

Prof. W. Huang
Key Laboratory of Flexible Electronics (KLOFE) & Institute of Advanced Materials (IAM)
Nanjing Tech University (NanjingTech)
Nanjing 211800, China

 The ORCID identification number(s) for the author(s) of this article can be found under <https://doi.org/10.1002/adma.201900526>.

DOI: 10.1002/adma.201900526

indicate that appropriate material design with regard to the crystalline lattice is a promising direction to acquire high-performance electrodes.^[19,20] As mentioned earlier, for a definite crystalline material, finding more beneficial active exposed facet with low energy barrier and stable ion-binding ability is very meaningful to reversely conjecture the optimized nanoscale manufacture process. To the best of our knowledge, the detailed research about the relationship between the different exposed facets and their corresponding pseudocapacitance response, as well as the Na⁺ storage properties, has rarely been noticed.

Tin (IV) sulfide (SnS₂), a typical layered material with hexagonal unit cell, possesses high theoretical capacity of 1136 mAh g⁻¹ based on both of the conversion and alloying processes.^[21] In this work, we employ a series of controllable and original programs, leading to three kinds of SnS₂ nanosheets involved in respectively “thinner” and “smaller” 3D shape evolution, virtually progressively exposing (001) and (100) facets. Furthermore, a kind of nitrogen and phosphorus codoped porous carbon (NPC) first developed by our group is adopted as a skeleton for the SnS₂ nanosheets loading, aiming to strengthen the electroconductivity and electrode stability of the anodes.^[22] As a result, the SnS₂ nanosheets with fully exposed active facets reveal the best Na⁺ storage performance among them. In addition, when we progressively expose the different active facets of SnS₂ nanosheets, the Na⁺ storage kinetics shows different variety regulation, generating various degrees of pseudocapacitance response and rate performance promotion. To explore the origin of this experimental fact, we also employ detailed density functional theory (DFT) calculations for the theoretical situations of Na storage and diffusion in SnS₂ crystalline structure.

Figure 1 shows the brief synthesis routes of the composites and overlooking scanning electron microscopy (SEM) images of the as-designed SnS₂ nanosheets. By smartly controlling the Sn sources, solvents, and reaction temperature, three kinds of SnS₂ nanosheets with stepwisely changed morphologies are

obtained, which are named as D-SnS₂, F-SnS₂, and SF-SnS₂, respectively (D: dozens layered; F: few layered; SF: small few layered). The NPC employed in this work can be not only served as the 3D skeleton to enhance the electroconductivity and strengthen the structural stability of the anodes, but also provide additional Na⁺ storage compared to common graphene and carbon nanotubes.^[23] Besides, from the lower magnification SEM images, it can be seen obviously that the SnS₂ nanosheets with “standing” feature are uniformly and fully anchored on the surface of NPC (Figure S1, Supporting Information). Figure 2 illustrates the detailed structure characterization and evolution of the three samples. As can be seen from Figure 2a–c, we draw three circles with radius of 100 nm in the TEM images, respectively, and the number of nanosheets situated in the circles shows an intuitively increasing trend in order, suggesting that the surface area density of the nanosheets on the NPC is improved through the reasonable synthetic adjustment. Figure 2d–f displays the high resolution transmission electron microscope (HRTEM) investigations of the three SnS₂ nanosheets, it can be clearly distinguished that the D-SnS₂ nanosheets are formed by more than 20 atom layers, as well as the F-SnS₂ and SF-SnS₂ are of around 10 layers. Based on the SEM and TEM images, it can be found that the F-SnS₂ and SF-SnS₂ become “thinner” and “smaller” compared to the D-SnS₂ and F-SnS₂, respectively (Figure 2g). Considering the 2D layered crystalline structure of SnS₂ (Figure S2, Supporting Information) and formation regulation of SnS₂ nanosheets, the essence of this two-step structure evolution is exposing the (001) and (100) facets of SnS₂ along the vertical directions. Furthermore, the HRTEM images of the three SnS₂ nanosheets display that the interplanar distances of (001) and (100) are around 0.59 and 0.32 nm, respectively (Figure S3, Supporting Information). Figure 2h shows the mapping test of SF-SnS₂@NPC, all of the expected elements of the composite can be recognized clearly.

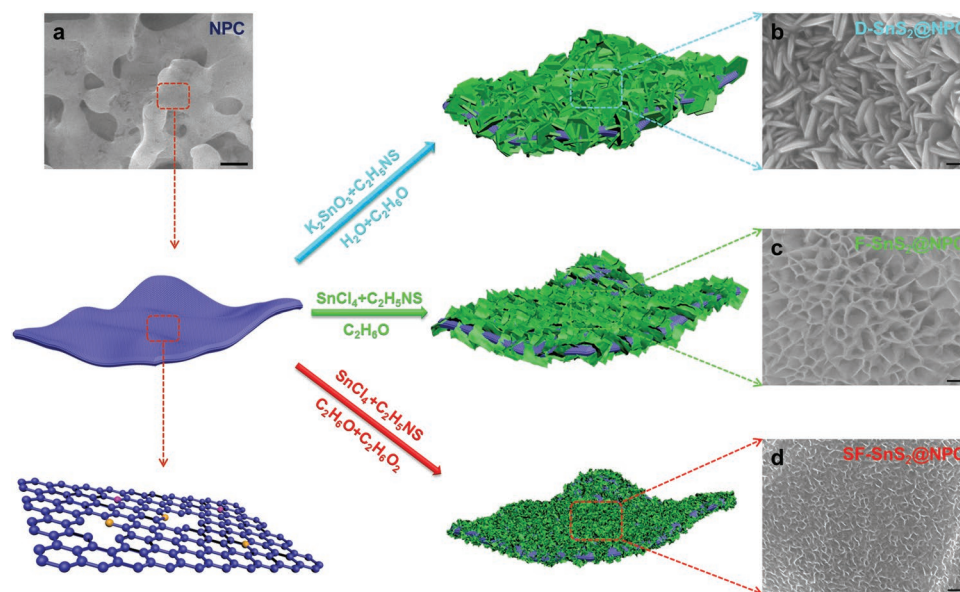


Figure 1. a) SEM image of the NPC substrate. b–d) SEM images of the as-designed D-SnS₂@NPC, F-SnS₂@NPC, and SF-SnS₂@NPC, respectively. Scale bars: a) 500 nm; b–d) 100 nm.

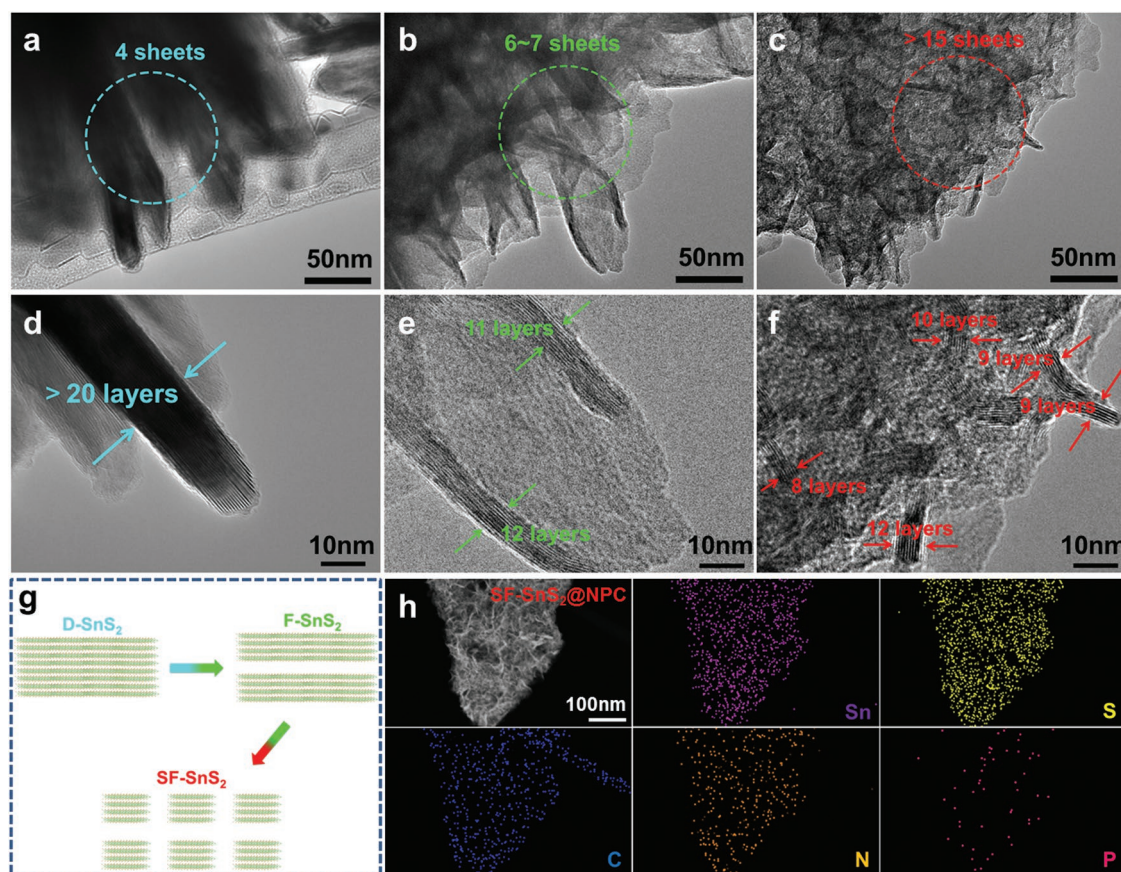


Figure 2. a–c) TEM and d–f) HRTEM images of the D-SnS₂@NPC (a,d), F-SnS₂@NPC (b,e), and SF-SnS₂@NPC (c,f). g) Structure evolution of the three SnS₂ nanosheets based on the SEM and TEM investigations. h) Elemental mapping images of the SF-SnS₂@NPC composite.

To obtain more crystal particulars of the different composite anodes, X-ray diffraction examinations are performed with the results of the three SnS₂@NPC samples shown in Figure S4 (Supporting Information), respectively. All of the apparent peaks are matched with the hexagonal structure (JCPDS card no. 23–0677), demonstrating the well crystallized 2T-type SnS₂. Furthermore, the (001) peaks of D-SnS₂@NPC, F-SnS₂@NPC, and SF-SnS₂@NPC are located at 14.96°, 14.80°, and 14.70°, respectively, which may be ascribed to the slight interlayer expansion trend of the different SnS₂ nanosheets.^[24–26] Thermogravimetric analysis tests are also employed to determine the mass constitution of the three SnS₂@NPC composites. By assuming the final calcined product in air atmosphere is SnO₂, the mass fraction of SnS₂ can be calculated to be 98.1%, 89.7%, and 90.0% for D-SnS₂@NPC, F-SnS₂@NPC, and SF-SnS₂@NPC, respectively (Figure S5, Supporting Information).^[27] To be more accurate, we investigate the SF-SnS₂@NPC sample by X-ray photoelectron spectroscopy, and the results are revealed in Figure S6 (Supporting Information). All of the related photoelectric peaks for Sn, S, C, N, P, and O can be distinguished from the survey spectrum clearly (Figure S6a, Supporting Information). Moreover, two strong peaks at 494.6 eV (Sn 3d_{3/2}) and 486.2 eV (Sn 3d_{5/2}) suggest that Sn⁴⁺ rather than Sn²⁺ exists in the as-prepared sample (Figure S6b, Supporting Information).^[28]

To investigate the detailed sodium-storage properties, **Figure 3** displays the rate capability and cycling performance

of the as-obtained SnS₂@NPC samples. Figure 3a presents the typical charge/discharge profiles of every SnS₂@NPC sample during the stable third loops at 0.1 A g⁻¹. In comparison, D-SnS₂@NPC shows the lowest discharge potential plateau and highest polarization among the three samples, indicating a relative higher energy barrier for Na⁺ ion diffusion in the SnS₂ layers.^[11,24] As a result, SF-SnS₂@NPC, F-SnS₂@NPC, and D-SnS₂@NPC anodes reveal gradually decreased reversible specific capacities of 823, 803, and 767 mAh g⁻¹, respectively. Further rate capabilities of the three SnS₂@NPC electrodes are also investigated with current densities varying from 0.1 to 12.8 A g⁻¹ (Figure 3b). As can be seen, the SF-SnS₂@NPC shows the smallest downward trend in specific capacities, and the relative capacity differences of the three SnS₂@NPC anodes present increasing tendency one by one during the turning up of current densities. Even at the maximum rate, the SF-SnS₂@NPC can still maintain a discharge capacity of 378 mAh g⁻¹. In addition, as shown in Figure 3c, the rate performance of the SF-SnS₂@NPC is also beneficial compared to most of the previously exhibited SnS₂ based anodes.^[27–37] Next, the capacity reversibility of three SnS₂@NPC composites and pure NPC skeleton is also tested at a constant current density of 0.2 A g⁻¹. Figure 3d reveals the representative sodiation/desodiation voltage curves of SF-SnS₂@NPC at 1st, 2nd, and 20th. The first discharge capacity of the composite is 1052 mAh g⁻¹ while resulting in a low Coulomb efficiency

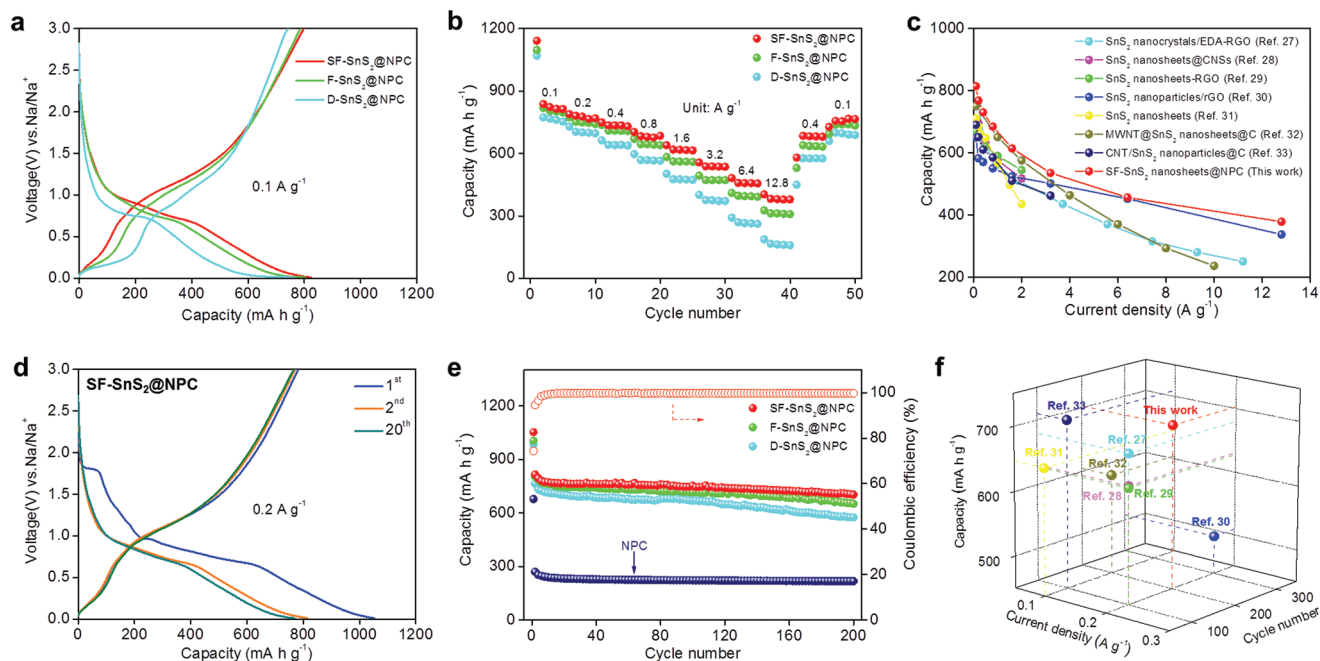


Figure 3. Electrochemical sodium-storage properties of $\text{SnS}_2@\text{NPC}$ anodes. a) The third galvanostatic charge–discharge voltage profiles of the three samples at 0.1 A g^{-1} . b) Rate performances of $\text{SnS}_2@\text{NPC}$ anodes at various current densities from 0.1 to 12.8 A g^{-1} . c) A comparison of rate capability with previously reported SnS_2 based anodes. d) Charge–discharge profiles of the SF- $\text{SnS}_2@\text{NPC}$ electrode at 0.2 A g^{-1} . e) Cycling performances of the $\text{SnS}_2@\text{NPC}$ samples together with pure NPC at 0.2 A g^{-1} , including the Coulombic efficiency of SF- $\text{SnS}_2@\text{NPC}$. f) A comparison of cycling performance with previously reported SnS_2 based anodes.

(CE) of 74%, which is common for metal oxide/sulfide based Li/Na ion batteries.^[38–40] After the first several cycles, the capacity decay of the $\text{SnS}_2@\text{NPC}$ anodes turns to much sluggish, indicating a relative remarkable structural stability of the as-prepared composites. Furthermore, the long term cycling performances of the three $\text{SnS}_2@\text{NPC}$ samples are illustrated in Figure 3e. As a result, the SF- $\text{SnS}_2@\text{NPC}$ is more robust compared to the other anodes and demonstrates the most stable cycling performance. Even after 200 cycles, a high discharge specific capacity of 701 mAh g^{-1} can still be preserved by SF- $\text{SnS}_2@\text{NPC}$ anode, resulting in an average capacity decay of 0.07% every cycle compared to the second discharge specific capacity. This fact proves that decreasing the thickness and size of the active SnS_2 nanosheets is beneficial for strengthening the stability of electrode. In addition, the pure NPC is able to show a good discharge capacity of around 220 mAh g^{-1} , which can also make a contribution for the as-prepared $\text{SnS}_2@\text{NPC}$ composites. Furthermore, the cycling capability of our SF- $\text{SnS}_2@\text{NPC}$ is also better than the previously introduced SnS_2 based anodes (Figure 3f).^[27–37] As a comparison, the pure SnS_2 nanoflakes display much more inferior cycling and rate performances than that of the three $\text{SnS}_2@\text{NPC}$ composites (Figure S7, Supporting Information). Furthermore, the three $\text{SnS}_2@\text{NPC}$ samples as well as pure SnS_2 nanoflakes are tested by Nyquist plots, the SF- $\text{SnS}_2@\text{NPC}$ and F- $\text{SnS}_2@\text{NPC}$ exhibit similar semicircle diameters, but much smaller than that of D- $\text{SnS}_2@\text{NPC}$ and pure SnS_2 nanoflakes, which are coincident with their sodium-storage performances (Figure S8, Supporting Information). The F- $\text{SnS}_2@\text{NPC}$ anode is also investigated after 50 cycles, as can be seen, the hierarchical morphology is able to be maintained,

thus proving the structural stability of the as-prepared SnS_2 nanosheets (Figure S9, Supporting Information).

According to the previous reported literatures, it is generally concluded that surface-controlled pseudocapacitive behavior of electrode possesses significant benefit for charge storage under high current density.^[41] Thus, to deeply understand the relationship between morphology evolution (crystalline facet exposing) and rate performance improvement, detailed quantitative kinetics investigation of the three $\text{SnS}_2@\text{NPC}$ anodes using cyclic voltammetry (CV) measurements is employed. As shown in Figure 4a and Figure S11 (Supporting Information), CV curves at progressively increased scan rates of the $\text{SnS}_2@\text{NPC}$ composites illustrate obvious discrepancy in both of anodic and cathodic peaks. To seek for more particulars about the changes of redox peaks, CV curves of the three $\text{SnS}_2@\text{NPC}$ samples at the same scan rate of 0.6 mV s^{-1} are compared in Figure 4b. It is notable that the anodic peak of F- $\text{SnS}_2@\text{NPC}$ is broader than that of D- $\text{SnS}_2@\text{NPC}$, and the peak current of SF- $\text{SnS}_2@\text{NPC}$ becomes larger compared to F- $\text{SnS}_2@\text{NPC}$. In another point of view, the D- $\text{SnS}_2@\text{NPC}$ and F- $\text{SnS}_2@\text{NPC}$ show almost same peak currents during anodic process, while the F- $\text{SnS}_2@\text{NPC}$ and SF- $\text{SnS}_2@\text{NPC}$ display similar shapes of anodic peaks. Due to the difference between the two shape change styles of the anodic peaks, it can be confirmed again that the two-step evolution of the SnS_2 nanosheets introduced in Figure 2g, that is, the stepwisely exposed crystalline facets of SnS_2 , possesses different influences on Na^+ transport and storage kinetics. It is generally accepted that the relationship between current (i) and sweep rate (ν) obeys the power-law equation: $i = a\nu^b$. When the value of b is equal to 0.5, a diffusion-dominated Na^+

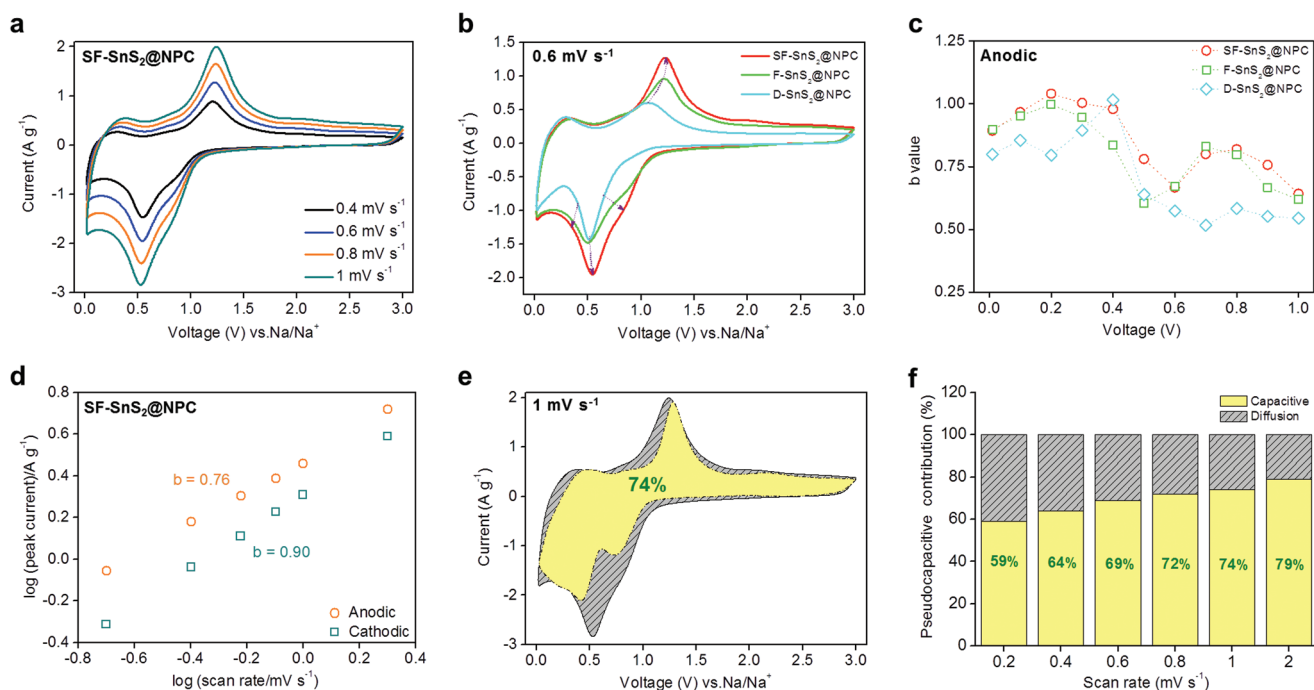


Figure 4. Kinetics and quantitative analysis of the Na⁺ storage behavior for SnS₂@NPC anodes. a) CV curves of SF-SnS₂@NPC at 0.4–1 mV s⁻¹. b) CV curves of the three SnS₂@NPC samples at 0.6 mV s⁻¹. c) Calculated *b* values of the three SnS₂@NPC anodes at different voltages during the anodic process. d) Logarithm peak current versus logarithm scan rate plots of SF-SnS₂@NPC. e) Separation of capacitive (yellow part) and diffusion (gray part) controlled contribution at 1 mV s⁻¹ for SF-SnS₂@NPC. f) Pseudocapacitive contribution ratio at a series of scan rates for SF-SnS₂@NPC.

intercalation mechanism is resulted, while the *b* value of 1 represents an extreme surface-controlled capacitive behavior. In particular, Figure 4c and Figure S12 (Supporting Information) display the comparison of calculated *b* values at intervals of 0.1 V, respectively, corresponding to anodic and cathodic reactions. Most of the *b* values are within the range of 0.5–1, thus proving that mixed Na⁺ storage mechanisms exist in these three kinds of anodes. Even more, the *b* values of D-SnS₂@NPC are evidently smaller than that of the other two samples, suggesting that increasing the number of exposed (001) facets is able to effectively improving the pseudocapacitance response of SnS₂ nanosheets. Figure 4d and Figure S13 (Supporting Information) show the linear relationships between logarithm peak currents and sweep rates based on the abovementioned power law equation. After calculations, it can be obtained that the *b* values of SF-SnS₂@NPC anode are closer to 1 than that of the other two composites (0.76 vs 0.69 vs 0.63 for the anodic peaks; 0.90 vs 0.81 vs 0.72 for the cathodic peaks). This fact further shows that increasing both of the exposed (001) and (100) facets of SnS₂ nanosheets can lead to more surface-controlled pseudocapacitive reactions with solvated Na⁺, which will make a considerable contribution to the energy storage at high rate.^[15,20] To be more exact, the quantitative capacitive-dominated (*i*₁) and diffusion-controlled (*i*₂) currents can be separated at the fixed potential by the next equation: $i = i_1 + i_2 = k_1v + k_2v^{1/2}$. As shown in Figure 4e and Figure S14 (Supporting Information), the capacitive-dominated areas (yellow part) are separated from the whole CV curves of the three anodes at 1 mV s⁻¹. Notably, the capacitive contribution of the F-SnS₂@NPC (≈68%; Figure S14a, Supporting Information) is closer to SF-SnS₂@

NPC (≈74%; Figure 4e) but much larger than that of D-SnS₂@NPC (≈55%; Figure S14c, Supporting Information). Furthermore, this phenomenon is also appearing in the other scan rates in view of the calculation results by the similar analysis method (Figure 4f; Figure S11b,d, Supporting Information).

According to the previous data, the Na⁺ storage performances of SnS₂ nanosheets are increased under varying degrees, accompanying with the turning into “thinner” and “smaller” processes, suggesting that exposing different facets generates dissimilar Na⁺ storage and diffusion kinetics. To understand this phenomenon more deeply, we employ DFT methods for the further calculations based on the first principles. Considering the former-mentioned structural evolution of the three SnS₂ nanosheets, we establish the optimized model structures of Na intercalated into the (001) interlayer and (100) lattice, as well as Na stored on the exposed (001) and (100) facets, which are shown in Figure 5a–d. As a result, the calculated binding energies (ΔE) of the four models are –0.86, –1.11, 15.30, and –2.32 eV (Figure 5e). It is thus concluded that Na atom intercalated into the (100) lattice shows an unstable status, due to the too narrow lattice spacing resulting in large energy barrier for Na intercalation. On the other hand, the binding stabilities of the Na storage on the exposed (100) and (001) facets are more stable than that of Na intercalated into the (001) interlayer, which further proves the important role for the surface-controlled Na⁺ storage compared to the diffusion-controlled process. In addition, the exposed (100) facet is more favorable for Na storage than that of exposed (001) facet. This result preliminarily explains the reason for different pseudocapacitive response and rate performance varieties during the two-step

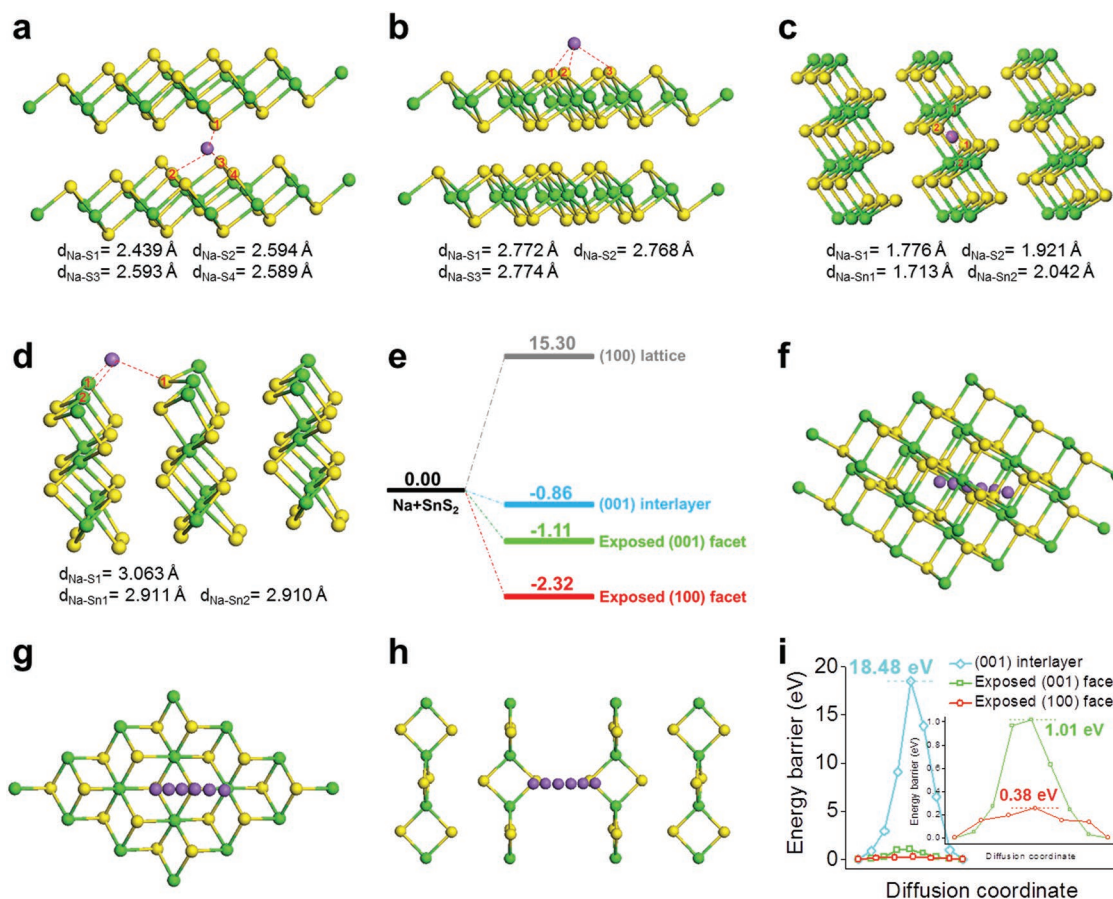


Figure 5. Theoretical simulations of Na storage and diffusion in SnS₂ crystal structure. a–d) Typical models of Na atom intercalated/adsorbed into/on the (001) interlayer (a), the exposed (001) facet (b), the (100) lattice (c), and the exposed (100) facet (d). e) Binding energies (ΔE , in eV) of the four Na–SnS₂ patterns. f–h) Typical models of Na atom diffusion paths in/on the (001) interlayer (f), the exposed (001) facet (g), and the exposed (100) facet (h). i) Na diffusion energy profiles through the different trajectories.

evolution of SnS₂ nanosheets. Moreover, we investigate the Na atom diffusion paths in/on the (001) interlayer, exposed (001) facet and exposed (100) facet (Figure 5f–h), with the Na diffusion energy profiles shown in Figure 5i. Similarly, the Na diffusion on the exposed (100) facet demonstrates the most ready route with the lowest energy barrier, which is consistent with the previous binding energy results. It is notable that the Na diffusion in the (001) interlayer generates much larger energy barrier than that of the other two diffusion styles, which further theoretically confirms that surface-controlled pseudocapacitive behavior is more advantageous than the diffusion-controlled Na⁺ storage process. From another point of view, stable binding status and low diffusion energy barrier are also beneficial to improve the structural stability of the electrode materials during the charge/discharge processes, leading to superior cycling performance. Considering the previous Na⁺ storage kinetics analysis results, the capacitive contributions of F-SnS₂@NPC are closer to SF-SnS₂@NPC, but much larger than that of D-SnS₂@NPC (for example, at 1 mV s⁻¹, 74% vs 68% vs 55%). This is because that the edge area of the nanosheets is much smaller than 2D face area, as a result, the total area of exposed (100) facets is also far smaller than that of exposed (001) facets. Thus, the above calculation results are well consistent with the

previous experimental outcomes, and strongly certificate the correctness of our structural design.

It is well known that during the low current density, the charging time is quite long and the anode materials are able to be fully charged by solvated Na⁺.^[42,43] Owing to the sluggish kinetics of Na⁺ solid state diffusion, during the increasing of the current rate, the Na⁺ storage and transportation processes are gradually limited, resulting in quick decreasing of specific capacity. Thus, the key point to relieve this issue is that improving the Na⁺ storage and diffusion kinetics by rational material structure design. To be more intuitional and based on the previous findings, as illustrated in **Figure 6**, the Na⁺ storage of crystalline SnS₂ at different charging situations is revealed. At the low rate, SnS₂ can be completely charged by deep Na⁺ intercalation between the interlayer, as well as the pseudocapacitive Na⁺ storage on the exposed (001) and (100) facets. When the charging rate is increased, the amount of Na⁺ stored in the interlayer shows a faster decreasing trend, compared to the surface-controlled Na⁺ storage. Until under the ultrahigh rate, the capacitive-controlled Na⁺ storage becomes more dominant but the Na⁺ intercalated in the interlayer turns to be further limited. Therefore, decreasing both of the thickness and size of the crystalline SnS₂ nanosheets can not only lower the Na⁺

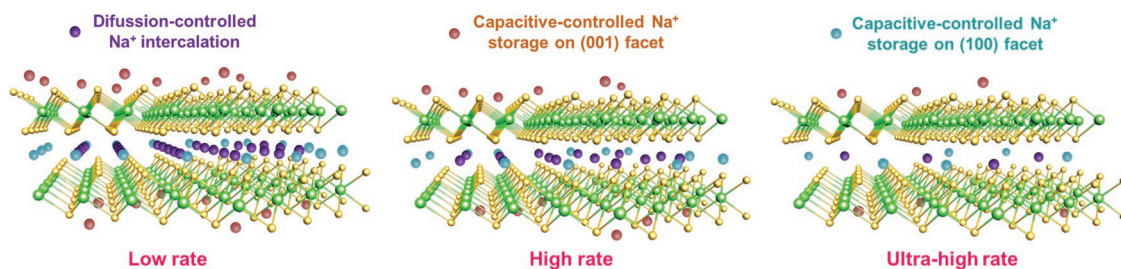


Figure 6. Schematic illustrating the Na⁺ storage mechanism of SnS₂ crystal structure. According to the abovementioned kinetics analysis and DFT calculation, it can be concluded that the SnS₂ can be fully charged both of the interlayers and exposed active facets under low current densities, but the capacitive-controlled Na⁺ storage on the exposed (100) and (001) facets will dominate more under high rate process.

diffusion energy barrier, but also provide more stable active facets for capacitive Na⁺ storage.

In summary, a series of SnS₂ nanosheets with progressively exposed (001) and (100) facets are successfully obtained by our reasonably designed synthesis processes, resulting in three kinds of SnS₂@NPC composites. After sodium-storage performance testing, the SF-SnS₂@NPC demonstrates better rate and cycling performances than the other two anodes, as well as many ever reported SnS₂ based electrode materials. More interestingly, kinetics analysis indicates that different exposed facets of crystalline SnS₂ nanosheets are able to generate dissimilar change styles of CV curves, as well as the corresponding pseudocapacitive contribution improvement trends. By means of the detailed DFT calculations about the Na storage and diffusion in SnS₂ crystal structure, we theoretically determine that the exposed facets possess more stable sites for Na storage, and lead to lower energy barriers during the Na diffusion. Furthermore, the exposed (100) facet is more favorable than exposed (001) facet for capacitive Na storage. In a word, our achievement demonstrates that exposed different crystalline facets are able to generate dissimilar Na⁺ storage and diffusion mechanisms. This conclusion can also be expanded to many other crystalline electrode materials, and help to explore the most proper structure design route, thus leading to the high-rate and stable metal-ions storage.

Supporting Information

Supporting Information is available from the Wiley Online Library or from the author.

Acknowledgements

This work was mainly supported by MoE Tier 1 (Grant No. RG19/17). W.H. thanks the supports by the National Basic Research Program of China-Fundamental Studies of Perovskite Solar Cells (Grant No. 2015CB932200), Natural Science Foundation of Jiangsu Province (Grant No. BM2012010), Priority Academic Program Development of Jiangsu Higher Education Institutions (Grant No. YX03001), Ministry of Education of China (Grant No. IRT1148), Synergetic Innovation Center for Organic Electronics and Information Displays, and the National Natural Science Foundation of China (Grant Nos. 61136003 and 51173081). H.Z. acknowledges the financial support from NTU under Start-Up Grant (Grant No. M4081296.070.500000), Joint Research Fund for Overseas Chinese, Hong Kong and Macao Scholars (Grant No. 51528201).

Conflict of Interest

The authors declare no conflict of interest.

Keywords

2D nanosheets, active facets, pseudocapacitance, sodium storage, tin (IV) sulfide

Received: January 22, 2019
Revised: February 20, 2019
Published online: March 11, 2019

- [1] N. Yabuuchi, K. Kubota, M. Dahbi, S. Komaba, *Chem. Rev.* **2014**, *114*, 11636.
- [2] P. Simon, Y. Gogotsi, B. Dunn, *Science* **2014**, *343*, 1210.
- [3] X. Xiang, K. Zhang, J. Chen, *Adv. Mater.* **2015**, *27*, 5343.
- [4] J. Sun, H. W. Lee, M. Pasta, H. Yuan, G. Zheng, Y. Sun, Y. Li, Y. Cui, *Nat. Nanotechnol.* **2015**, *10*, 980.
- [5] M. Lao, Y. Zhang, W. Luo, Q. Yan, W. Sun, S. X. Dou, *Adv. Mater.* **2017**, *29*, 1700622.
- [6] H. Hou, X. Qiu, W. Wei, Y. Zhang, X. Ji, *Adv. Energy Mater.* **2017**, *7*, 1602898.
- [7] J. Y. Hwang, S. T. Myung, Y. K. Sun, *Chem. Soc. Rev.* **2017**, *46*, 3529.
- [8] H. Zhang, I. Hasa, S. Passerini, *Adv. Energy Mater.* **2018**, *8*, 1702582.
- [9] X. Xu, C. Niu, M. Duan, X. Wang, L. Huang, J. Wang, L. Pu, W. Ren, C. Shi, J. Meng, B. Song, L. Mai, *Nat. Commun.* **2017**, *8*, 460.
- [10] K. Zhang, M. Park, L. Zhou, G. H. Lee, J. Shin, Z. Hu, S. L. Chou, J. Chen, Y. M. Kang, *Angew. Chem., Int. Ed.* **2016**, *55*, 12822.
- [11] X. Xu, R. Zhao, W. Ai, B. Chen, H. Du, L. Wu, H. Zhang, W. Huang, T. Yu, *Adv. Mater.* **2018**, *30*, 1800658.
- [12] C. Chen, Y. Wen, X. Hu, X. Ji, M. Yan, L. Mai, P. Hu, B. Shan, Y. Huang, *Nat. Commun.* **2015**, *6*, 6929.
- [13] Y. Fang, X. Y. Yu, X. W. Lou, *Adv. Mater.* **2018**, *30*, 1706668.
- [14] V. Augustyn, J. Come, M. A. Lowe, J. W. Kim, P. L. Taberna, S. H. Tolbert, H. D. Abruña, P. Simon, B. Dunn, *Nat. Mater.* **2013**, *12*, 518.
- [15] D. Chao, C. Zhu, P. Yang, X. Xia, J. Liu, J. Wang, X. Fan, S. V. Savilov, J. Lin, H. J. Fan, *Nat. Commun.* **2016**, *7*, 12122.
- [16] J. B. Cook, H. S. Kim, T. C. Lin, C. H. Lai, B. Dunn, S. H. Tolbert, *Adv. Energy Mater.* **2017**, *7*, 1601283.
- [17] V. Augustyn, P. Simon, B. Dunn, *Energy Environ. Sci.* **2014**, *7*, 1597.

- [18] Y. Xiao, P. F. Wang, Y. X. Yin, Y. F. Zhu, Y. B. Niu, X. D. Zhang, J. Zhang, X. Yu, X. D. Guo, B. H. Zhong, Y. G. Guo, *Adv. Mater.* **2018**, *30*, 1803765.
- [19] K. J. Griffith, K. M. Właderek, G. Cibin, L. E. Marbella, C. P. Grey, *Nature* **2018**, 559, 556.
- [20] H. S. Kim, J. B. Cook, H. Lin, J. S. Ko, S. H. Tolbert, V. Ozolins, B. Dunn, *Nat. Mater.* **2017**, *16*, 454.
- [21] T. Zhou, W. K. Pang, C. Zhang, J. Yang, Z. Chen, H. K. Liu, Z. Guo, *ACS Nano* **2014**, *8*, 8323.
- [22] W. Ai, X. Wang, C. Zou, Z. Du, Z. Fan, H. Zhang, P. Chen, T. Yu, W. Huang, *Small* **2017**, *13*, 1602010.
- [23] X. Xu, D. Yu, H. Zhou, L. Zhang, C. Xiao, C. Guo, S. Guo, S. Ding, *J. Mater. Chem. A* **2016**, *4*, 4375.
- [24] Z. Hu, L. Wang, K. Zhang, J. Wang, F. Cheng, Z. Tao, J. Chen, *Angew. Chem., Int. Ed.* **2014**, *53*, 12794.
- [25] M. A. Tsiamtsouri, P. K. Allan, A. J. Pell, J. M. Stratford, G. Kim, R. N. Kerber, P. C. M. Magusin, D. A. Jefferson, C. P. Grey, *Chem. Mater.* **2018**, *30*, 1505.
- [26] D. Chao, P. Liang, Z. Chen, L. Bai, H. Shen, X. Liu, X. Xia, Y. Zhao, S. V. Savilov, J. Lin, *ACS Nano* **2016**, *10*, 10211.
- [27] Y. Jiang, M. Wei, J. Feng, Y. Ma, S. Xiong, *Energy Environ. Sci.* **2016**, *9*, 1430.
- [28] Y. Liu, X. Y. Yu, Y. Fang, X. Zhu, J. Bao, X. Zhou, X. W. Lou, *Joule* **2018**, *2*, 725.
- [29] B. Qu, C. Ma, G. Ji, C. Xu, J. Xu, Y. S. Meng, T. Wang, J. Y. Lee, *Adv. Mater.* **2014**, *26*, 3854.
- [30] Y. Zhang, P. Zhu, L. Huang, J. Xie, S. Zhang, G. Cao, X. Zhao, *Adv. Funct. Mater.* **2015**, *25*, 481.
- [31] W. Sun, X. Rui, D. Yang, Z. Sun, B. Li, W. Zhang, Y. Zong, S. Madhavi, S. Dou, Q. Yan, *ACS Nano* **2015**, *9*, 11371.
- [32] B. Luo, Y. Hu, X. Zhu, T. Qiu, L. Zhi, M. Xiao, H. Zhang, M. Zou, A. Cao, L. Wang, *J. Mater. Chem. A* **2018**, *6*, 1462.
- [33] Y. Zhao, B. Guo, Q. Yao, J. Li, J. Zhang, K. Hou, L. Guan, *Nanoscale* **2018**, *10*, 7999.
- [34] Y. Liu, H. Kang, L. Jiao, C. Chen, K. Cao, Y. Wang, H. Yuan, *Nanoscale* **2015**, *7*, 1325.
- [35] J. Wang, C. Luo, J. Mao, Y. Zhu, X. Fan, T. Gao, A. C. Mignerey, C. Wang, *ACS Appl. Mater. Interfaces* **2015**, *7*, 11476.
- [36] P. V. Prikhodchenko, D. Y. W. Yu, S. K. Batabyal, V. Uvarov, J. Gun, S. Sladkevich, A. A. Mikhaylov, A. G. Medvedev, O. Lev, *J. Mater. Chem. A* **2014**, *2*, 8431.
- [37] X. Xie, D. Su, S. Chen, J. Zhang, S. Dou, G. Wang, *Chem. - Asian J.* **2014**, *9*, 1611.
- [38] N. Wang, X. Xu, T. Liao, Y. Du, Z. Bai, S. Dou, *Adv. Mater.* **2018**, *30*, 1804157.
- [39] Y. Liu, H. Wang, L. Cheng, N. Han, F. Zhao, P. Li, C. Jin, Y. Li, *Nano Energy* **2016**, *20*, 168.
- [40] Z. Zhang, H. Zhao, Y. Teng, X. Chang, Q. Xia, Z. Li, J. Fang, Z. Du, K. Swierczek, *Adv. Energy Mater.* **2018**, *8*, 1700174.
- [41] H. Sun, L. Mei, J. Liang, Z. Zhao, C. Lee, H. Fei, M. Ding, J. Lau, M. Li, C. Wang, X. Xu, G. Hao, B. Papandrea, I. Shakir, B. Dunn, Y. Huang, X. Duan, *Science* **2017**, *356*, 599.
- [42] Z. Li, J. Ding, D. Mitlin, *Acc. Chem. Res.* **2015**, *48*, 1657.
- [43] P. Gao, Y. Y. Zhang, L. Wang, S. Chen, Y. Huang, X. Ma, K. Liu, D. Yu, *Nano Energy* **2017**, *32*, 302.